Multibody System Dynamics
https://doi.org/10.1007/s11044-024-09980-6

RESEARCH

A new contact and road model for multi-body dynamic simulation of wheeled vehicles on soft-soil terrain

Evangelos Koutras[1] · Felipe Moretti Leila[2] · Adrijan Ribaric[2] · Sotirios Natsiavas[1]

Received: 14 November 2023 / Accepted: 14 March 2024

Abstract
In this paper, a new high-performance and memory-efficient contact and road model is developed. Specifically, the road is modeled as a rectangular structured grid of deformable springs in the vertical direction, thus enabling fast execution. The new road model stands out due to its ability to handle large road scenarios by allocating computer memory dynamically for each spring, resulting in efficient memory utilization. Furthermore, each spring represents a small road patch that entails various information, such as the soil elevation, the soil properties, and the soil compaction, allowing for complicated simulations incorporating spatially varying soil properties and phenomena related to the multi-pass effect. In addition, using the new contact model, complex terrain geometries are handled in a computationally efficient way by approximating locally the irregular road profile with a suitable equivalent plane. For this, two different strategies are proposed, namely the radial basis function (RBF) interpolation method and the 3D enveloping contact model. Finally, the proposed techniques are implemented in Altair MotionSolve, a comprehensive multi-body simulation software for complex mechanical systems. In particular, a single-wheel test bed is initially examined followed by a four-wheeled rover model and the next-generation NATO reference mobility model (NG-NRMM). In all cases, the proposed model is validated by using available experimental data. Lastly, a case involving both wheeled and tracked vehicles is also examined by using a shared road model.

Keywords Soft soil · Contact model · Road model · Terramechanics · Wheeled vehicles

1 Introduction

The tire/soft-soil interaction and the corresponding modeling is of utmost importance to properly predict the mobility of vehicles in a wide range of engineering applications, such as agricultural machines [1], planetary explorations rovers [2, 3] as well as construction, mining, and military vehicles [4]. Therefore, a significant amount of research effort has been concentrated during the last years on developing appropriate contact and road models

✉ S. Natsiavas
natsiava@auth.gr

[1] Department of Mechanical Engineering, Aristotle University, 54124, Thessaloniki, Greece

[2] Altair Engineering Inc., 1820 E. Big Beaver Rd, Troy MI, 48083, USA

Published online: 04 April 2024

for the corresponding interaction. The modeling techniques of this interaction can be split into two broad categories: a) high-fidelity physics models; b) and semi-empirical models [5].

In the first category, a high degree of accuracy can, generally, be achieved with the drawback of significantly increased computational resources necessary for the simulation. Typical applications include the use of discrete element method (DEM) [6, 7] as well as the finite element method (FEM) [8, 9] for the simulation of the soil material. In addition, the use of smoothed particle hydrodynamics (SPH) method has been recently proposed for describing the granular dynamics [10, 11].

Alternatively, the core idea of semi-empirical models is founded on empirical and analytical equations, which are based on experimental observations. Therefore, a lower degree of accuracy is, usually, achieved due to the underlying assumptions present in these models. However, the use of analytical expressions results in fast execution in addition to low memory allocation of the simulation code. This makes these models more suitable for use in multi-body and vehicle simulations in general. Therefore, the focus is placed on semi-empirical models in this work.

In semi-empirical models, the emphasis is, initially, placed on properly describing the pressure-sinkage and the shear stress-shear displacement relationship through analytical expressions. More specifically, the model proposed by Bekker [12, 13] constitutes a cornerstone for describing the pressure-sinkage relationship. Subsequently, this model has been extended by Wong and Reece [14] to include the distribution of both radial and tangential stresses and, thus, their influence on the resulting forces at the wheel-soil interface.

In the meantime, Janosi and Hanamoto [15] developed a model for the definition of the shear stress-shear displacement relationship. Specifically, an exponential function in addition to a new constant, the shear modulus, is employed for describing the shear stress-shear displacement relationship based on the Mohr–Coulomb failure criterion. For the limiting case of very large soil displacement values, the proposed model predicts that there is a threshold for the resulting shear stress based solely on this failure criterion.

Apparently, until this point, the models are purely 2D, thus only the longitudinal and the vertical force as well as the rolling resistance torque can be calculated. Subsequently, the steering characteristics have been examined from Yoshida and Ishigami [16, 17]. In particular, the soil deformation in the lateral (y) direction has been established in [16] in a similar way to the deformation in the longitudinal (x) direction [14]. Moreover, the lateral force comprises two different parts, namely the force produced by the shear stress underneath the wheel and the reaction force due to the bulldozing effect on the side face of the wheel [16, 17].

Furthermore, the multi-pass effect is of utmost importance to properly predict the mobility of vehicles on soft-soil terrain. For this, a model for describing the response of the soil to repetitive normal loading was proposed by Wong [18] based on experimental observations. Following that, the core idea of this model was adopted by Harnisch et al. [19] and by Sandu et al. [20]. Conversely, in [21] a different route was followed. In particular, the soil properties are modified after each pass and the corresponding variations are functions of the slip, based on the existing experimental data [22].

In addition, a methodology for incorporating the tire deformability has been developed in [19]. For this, a larger substitute circle is used to describe the resulting tire–soil contact patch area due to the tire's deformation. It should be mentioned that the underlying idea was first proposed by Bekker [13] but has never been carried out due to the complexity of the calculations. Moreover, in the same paper [19], the maximum shear stress for a given pressure is modified by taking into account the coefficient of friction at the wheel–soil interface.

Overall, the new modeling approach acts as a bridge between the classical and well-established principles introduced by Bekker/Wong/Janosi and Hanamoto and the current capabilities of multi-body system solvers. More specifically, based on these principles, a new, fast, and memory-efficient road and contact model is developed here. Using the new techniques, a full, three-dimensional (3D) modeling of the tire/soft-soil interaction is achieved, enabling the use of complex terrain geometries and the execution of complicated simulations incorporating spatially varying soil properties and the phenomena related to the multi-pass effect.

For this, the road model needs to be spatially discretized to enable the use of complex, irregular terrain geometries. Therefore, in this work, the road is represented as a rectangular structured grid, which can deform in the vertical direction. It should be noted that similar approaches have been developed in [5, 20, 23, 24], which constitute the basis for the new road model. In particular, the soil contact model (SCM) proposed in [23] uses a digital elevation map (DEM) to define the soil surface topology based on a uniformly spaced horizontal mesh grid and constant mesh size. Following that, the SCM model was extended by Tasora et al. [5] to work with nonstructured triangle meshes, while including an optional automatic refinement of the level of detail. In addition, a high-resolution height-field (HF) is employed in [24] for the terrain representation to consider irregularities in the terrain surface. The present paper is focused on soft soil and off-road scenarios. Thus, it should be clarified that the examined road model corresponds to soft soil and deformable terrains.

However, the rectangular grid structure employed here results in fast execution of the simulation code. Moreover, a distinct feature of the new road model stems from its ability to handle large road scenarios. More specifically, the overhead on computer memory is kept to a minimum by allocating the necessary memory for each spring when it is first needed. In addition, the height-field data structure is augmented with the soil properties and the soil history parameters in this work. Consequently, advanced simulations incorporating spatially varying soil properties as well as phenomena related to the multi-pass effect can be properly carried out by utilizing the new road model.

Moreover, a high-performance tire/soil contact model, which enables the use of complex, irregular terrain profiles, is proposed here. Specifically, the necessary calculations for the tire–soil interaction are not performed on a per node basis in this work, as is mainly the case in the literature [5, 20, 23]. Instead, the irregular terrain geometry underneath each tire is locally approximated with a proper equivalent plane here. Therefore, a simple wheel/plane intersection problem is derived, which can be resolved in a much easier and computationally efficient way.

It should be noted that a similar approach has been developed by Azimi et al. by utilizing a least-squares plane [24, 25]. Herein, two new strategies for deriving the equivalent plane are proposed. In particular, the radial basis function interpolation method [26] is initially employed. Using this approach, a local or global response can be achieved depending on the radial basis function used. Therefore, a prominent feature of this contact model lies in its ability to easily adapt to the application's needs based on the selection of the radial basis function. Moreover, using this method, the local inclinations of the road surface can be determined in an analytical and efficient way [27].

Following that, a well-established and widely used contact model for rough nondeformable (rigid) terrain, namely the 3D enveloping method [28, 29], is used. The core idea of this method is founded on using a series of ellipses to scan the road profile and, thus, produce an effective road plane. Therefore, the same technique is employed here for deriving an equivalent plane that locally approximates the irregular profile of a deformable terrain since, to the best of the authors' knowledge, this methodology has not been examined from this point of view.

In addition, a variety of vehicle models are used for testing the new techniques proposed in this work. For this, the proposed methods are implemented in Altair MotionSolve, a comprehensive multi-body simulation software for complex mechanical systems. Subsequently, a single-wheel test bed is initially used to confirm the validity of the single tire's longitudinal and lateral forces under combined slip conditions. Following that, the developed methods are tested in various advanced simulations to illustrate their effectiveness and applicability in real-life engineering applications. Specifically, a four-wheeled planetary exploration rover and the FED-Alpha vehicle of the next generation NATO reference mobility model [30, 31] are tested in various complex maneuvers. Lastly, a case involving a wheeled utility terrain vehicle (UTV) and a tracked personnel carrier vehicle is handled by introducing the concept of a shared road model.

The organization of this paper is as follows. First, the new road model is presented along with a description of obstacles' definition. Following that, the core idea of the new contact model is introduced, while a thorough description of the two different strategies is carried out next. In particular, the equations for the radial basis function interpolation method and the 3D enveloping contact model are formulated. Subsequently, the theoretical approach of this paper is completed by displaying the essential parts of the tire/soft-soil interaction. Then, the examined models are presented along with the extracted numerical results that demonstrate the validity and effectiveness of the proposed methods. Finally, the most important conclusions are summarized in the last section.

2 Road modeling

Within this work, the road surface is represented by a height-field (HF), thus enabling the use of rough terrain geometries. Specifically, a rectangular structured grid of deformable springs in the vertical (z-axis) direction is used, as shown in Fig. 1. Based on this approach, each spring represents a small road patch for which the necessary information is stored. The properties of each spring include the soil elevation (z coordinate), the soil properties, and the information regarding the compaction of the soil. Therefore, the HF data structure is augmented with the soil properties and the soil compaction parameters, as depicted in Fig. 1. This allows the execution of advanced simulations incorporating spatially varying soil properties and phenomena related to the multi-pass effect by using the new road model.

In addition, a constant grid spacing is used for the description of the road surface, which is set automatically based on the minimum tire width present in the model. This approach has been preferred over the case of nonstructured grids since the rectangular grid structure used here results in fast execution of the simulation code. This stems from the fact that, given specific x and y coordinates, the current spring can be identified in an extremely easy and computationally efficient way since a constant grid spacing is used for the whole soil area.

In general, this approach comes with the drawback of significantly increased memory allocation since the road discretization must be the same even for soil areas that the vehicle will not interact with. Therefore, a proper treatment for this issue is also proposed in this work. Specifically, in a wide range of applications, it is necessary to predict the vehicle mobility over a large soil area. In these cases, it would be extremely inefficient to allocate the necessary memory for the whole grid of springs from the beginning of the simulation. A distinct feature of the new road model lies in its ability to handle such cases by allocating the memory needed for the springs when it is first needed. Specifically, each spring is created, and the corresponding properties are stored when it gets pressed for the first time, thus leading to greatly improved memory allocation of the simulation code.

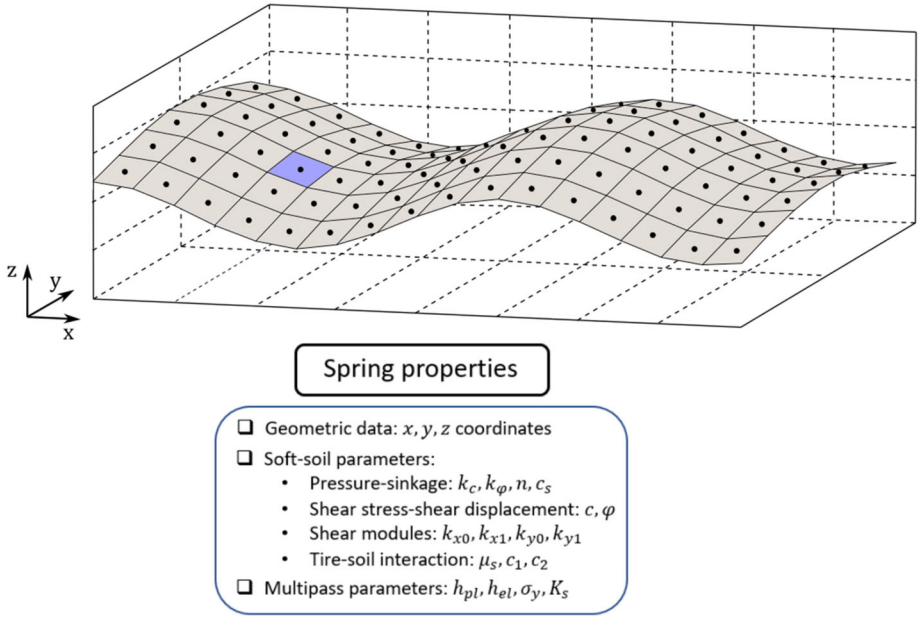

Fig. 1 Road modeled as an HF data structure, augmented with the soft-soil properties and multi-pass parameters

2.1 Obstacle definition

Using this road model, it is possible to define generic-shaped obstacles, while the option to assign different soft-soil properties (compared to the whole soil area) for the obstacle's region is also enabled. In particular, a variety of predefined obstacle templates can be readily used, which are superimposed on the existing soft-soil road profile. For this, a few basic parameters, including their dimensions and their position and orientation, are the only essential input data for their definition, as shown in Fig. 2.

Within this soft-soil tire model, the following obstacle types can be created:

- Rectangular obstacle
- Circular obstacle
- Bump obstacle
- Ramp obstacle
- Roof obstacle
- Sine obstacle
- Sine-sweep obstacle (linear/logarithmic)
- Plank obstacle (beveled edges/round edges)
- Arbitrary obstacle

More specifically, using the last option, a generic obstacle can be created, as depicted in Fig. 3, where the obstacle's region can have an arbitrary shape. A rectangular grid structure is still used for the road model, while an irregular terrain surface can be defined inside the obstacle's region by assigning proper soil elevation (z) values to the enclosed springs. Furthermore, in all cases, it is possible to assign different soft-soil properties for the obstacle's enclosing area by creating a new material that includes all the necessary parameters. Lastly,

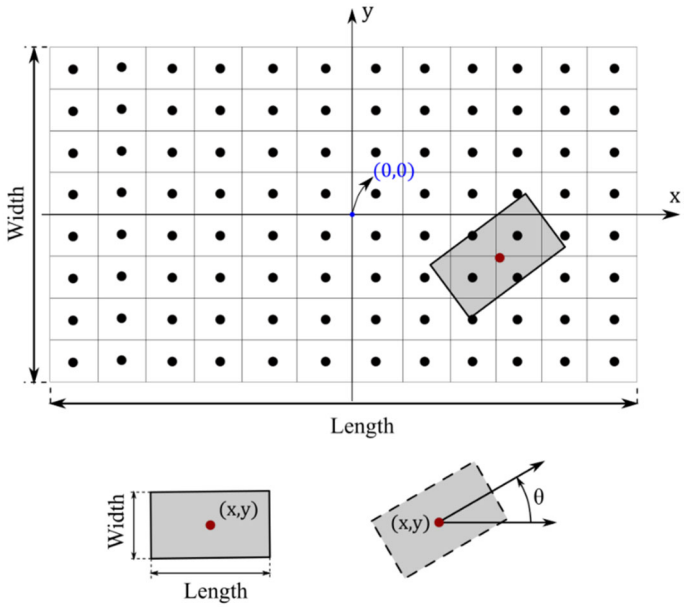

Fig. 2 Obstacle's geometry, superimposed on the existing soft-soil road profile

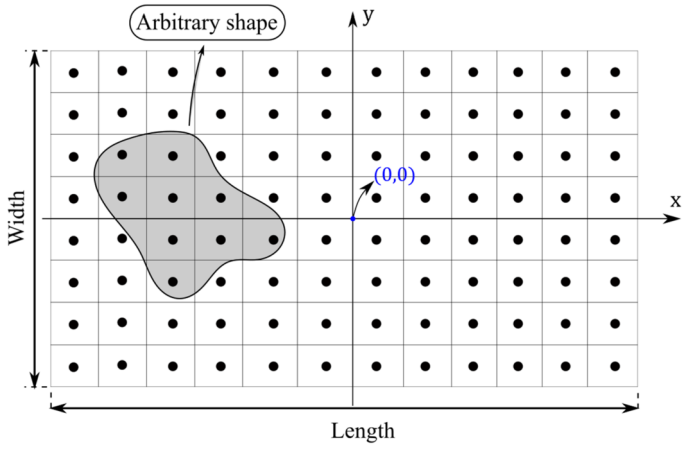

Fig. 3 Arbitrary obstacle, superimposed on the existing soft-soil road profile

each obstacle can also be identified as rigid, thus leading to a tire-rigid road interaction. In such cases, a well-established tire model for rigid road, namely the Fiala tire model, is used to model the corresponding interaction.

2.2 Shared road model

At this point, it is worth noting that the new road model can also be used for predicting the mobility of tracked vehicles on soft-soil terrain. This allows the analysis of cases where both

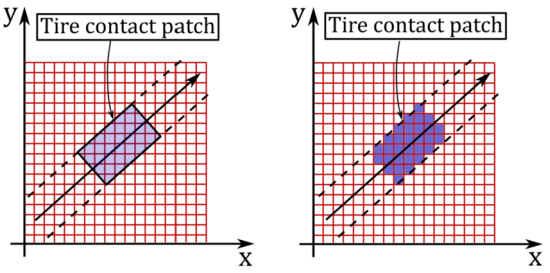

Fig. 4 Tire–soil contact patch and springs enclosed in the tire contact patch area

wheeled and tracked vehicles co-exist in a model and, thus, a shared road model must be used since the mobility of each vehicle is strongly influenced by the soil compaction created by the other vehicles. For this, the same set of soft-soil parameters is used for both cases, while the soil compaction parameters are updated after each pass of the wheels or the track links.

3 Contact modeling

Concerning the tire–soil contact model, a computationally efficient approach is developed here, which enables the use of irregular terrain profiles. Specifically, instead of performing the necessary calculations for the tire–soil interaction on a per-node basis, the rough terrain surface is locally approximated with a proper equivalent plane. Therefore, a much faster execution of the simulation code is achieved since the complexity of the examined contact problem is significantly reduced.

In particular, two contact methods are developed and presented in this work, namely the radial basis function (RBF) interpolation method and the 3D enveloping contact model. However, the core idea in both models remains the same. That is, based on the above-described methodology, both contact models use the springs enclosed in the tire contact patch area (see Fig. 4) to calculate the equivalent soil elevation and local inclinations of the road surface.

3.1 Radial basis function (RBF) interpolation

In the first case, a radial basis function interpolation process [26] is employed to calculate representative values for the soil elevation and the partial derivatives of the road surface. For this, assuming that the tire–soil contact patch area consists of n spring regions with coordinates $\left(\underline{x}_i = (x_i, y_i), z_i\right)$, $i = 1, \ldots, n$, the weights w_i, $i = 1, \ldots, n$, are initially determined using the equations

$$z\left(\underline{x}_j\right) = \sum_{i=1}^{n} w_i \varphi\left(r_{ij}\right), \quad j = 1, \ldots, n, \tag{1}$$

where the distance r_{ij} is given by

$$r_{ij} = \left\| \underline{x}_j - \underline{x}_i \right\| \tag{2}$$

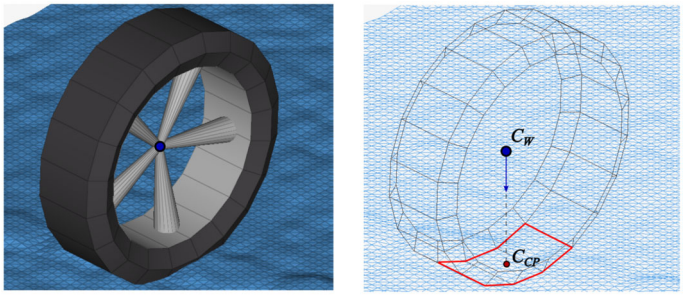

Fig. 5 Three-dimensional contact patch area and projection of wheel center on the road surface

and φ is a radial basis function. The system of equations (Eq. (1)) can be written in the equivalent matrix form:

$$\begin{bmatrix} \varphi\left(\left\|\underline{x}_0-\underline{x}_0\right\|\right) & \varphi\left(\left\|\underline{x}_0-\underline{x}_1\right\|\right) & \cdots & \varphi\left(\left\|\underline{x}_0-\underline{x}_n\right\|\right) \\ \varphi\left(\left\|\underline{x}_1-\underline{x}_0\right\|\right) & \varphi\left(\left\|\underline{x}_1-\underline{x}_1\right\|\right) & \cdots & \varphi\left(\left\|\underline{x}_1-\underline{x}_n\right\|\right) \\ \vdots & \vdots & \ddots & \vdots \\ \varphi\left(\left\|\underline{x}_n-\underline{x}_0\right\|\right) & \varphi\left(\left\|\underline{x}_n-\underline{x}_1\right\|\right) & \cdots & \varphi\left(\left\|\underline{x}_n-\underline{x}_n\right\|\right) \end{bmatrix} \begin{pmatrix} w_0 \\ w_1 \\ \vdots \\ w_n \end{pmatrix} = \begin{pmatrix} z\left(\underline{x}_0\right) \\ z\left(\underline{x}_1\right) \\ \vdots \\ z\left(\underline{x}_n\right) \end{pmatrix}. \tag{3}$$

Following that, the interpolated value for the soil elevation is derived by using the equation

$$z\left(\underline{x}\right)=\sum_{i=1}^{n} w_i \varphi\left(\left\|\underline{x}-\underline{x}_i\right\|\right). \tag{4}$$

It is worth noting that a significant advantage of the RBF method lies in its ability to work both with structured and nonstructured grids. In addition, this contact model can be used as a general framework for the calculation of the equivalent plane, depending on the radial basis function used. More specifically, typical radial basis functions that can be used include the Gaussian, the multiquadric, and the inverse multiquadric function, which are provided by the following expressions:

$$\text{Gaussian:} \quad \varphi\left(r\right)=e^{-(\varepsilon r)^2}, \tag{5}$$

$$\text{Multiquadric:} \quad \varphi\left(r\right)=\sqrt{1+(\varepsilon r)^2}, \tag{6}$$

$$\text{Inverse multiquadric:} \quad \varphi\left(r\right)=\frac{1}{\sqrt{1+(\varepsilon r)^2}}. \tag{7}$$

In the above equations, the position vector $\underline{x}=(x, y)$ corresponds to the point C_{CP} of the tire contact patch area, as shown in Fig. 5. This point is derived by projecting the wheel center C_W on the road surface by taking into account the wheel orientation. In addition, ε represents the shape parameter that controls the flatness of the different radial basis functions. Herein, the shape parameter is calculated based on the average distance between the springs enclosed in the contact patch area.

Apparently, the Gaussian and inverse multiquadric radial basis functions exhibit a local response since their value decreases with increasing distance r, as illustrated in Fig. 6. Conversely, the value of the multiquadric function increases with increasing distance, thus a

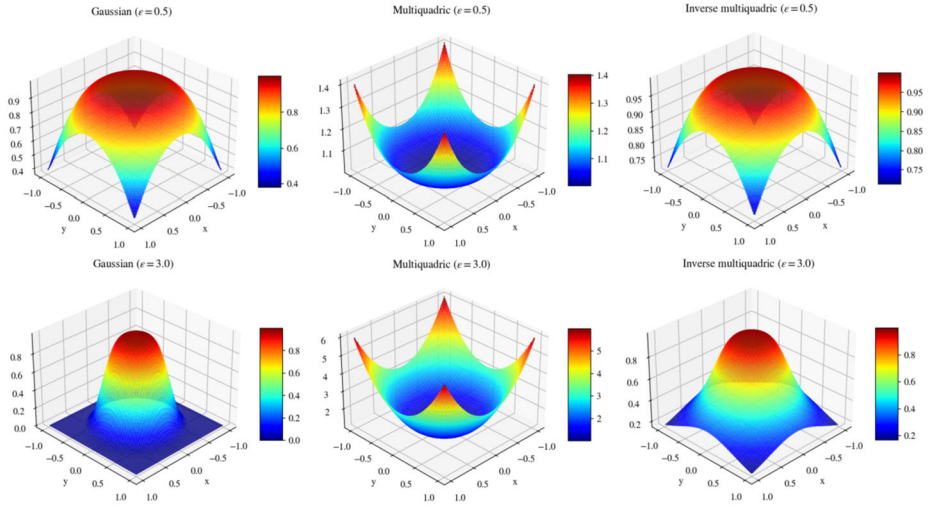

Fig. 6 Gaussian, multiquadric and inverse multiquadric radial basis functions' values for $\varepsilon = 0.5$ *and* $\varepsilon = 3$

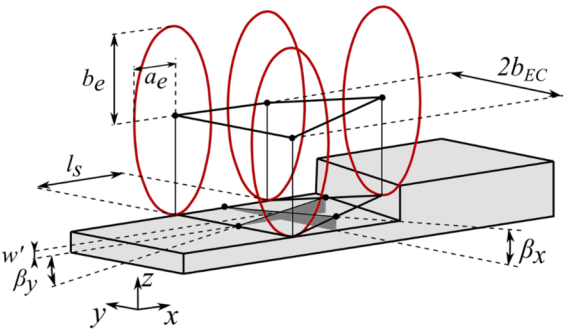

Fig. 7 3D enveloping contact model (*Reproduced from* [28])

global response is achieved. Therefore, a prominent feature of this contact model stems from its ability to easily adapt on the application's needs, based on the selection of the radial basis function. In addition, using this contact model, the local inclinations of the road surface are calculated in an analytical and efficient way [27].

3.2 3D enveloping contact model

Concerning the second contact model, the 3D enveloping method is a well-established model for irregular nondeformable (rigid) terrain [28, 29]. In this paper, the same technique is applied to construct an effective plane, which, locally, approximates the irregular profile of a deformable terrain. The core idea is founded on using a series of ellipses to scan the road profile and, thus, to produce an effective road plane that is defined by three quantities. Namely, the modified effective height w', the effective forward slope β_y, and the effective road camber angle β_x. The simplest form of this contact model is depicted in Fig. 7.

Specifically, the shape of the ellipses is defined by the parameters a_e, b_e, and c_e according to the expression

$$\left(\frac{x}{a_e}\right)^{c_e} + \left(\frac{z}{b_e}\right)^{c_e} = 1. \tag{8}$$

These parameters are calculated by introducing the user-defined dimensionless parameters [28]

$$p_{ae} = \frac{a_e}{R}, \tag{9}$$

$$p_{be} = \frac{b_e}{R}, \tag{10}$$

$$p_{ce} = c_e. \tag{11}$$

In addition, the tandem base length l_s is defined by introducing the user-defined dimensionless parameter

$$p_{ls} = \frac{l_s}{2a}, \tag{12}$$

where $2a$ denotes the length of the tire contact patch, while the parameter $2b_{EC}$ corresponds to the tire's width. Once the necessary parameters are defined, the height of the center of each ellipsis Z is calculated at every time point by scanning the road profile underneath the ellipsis and determining the corresponding height based on the ellipsis–road intersection. A thorough presentation of the underlying theory in addition to guidelines for the selection of the associated parameters can be found in [28].

In this simple form of the 3D enveloping contact model, the necessary quantities are calculated by using the equations

$$w' = \frac{Z_{f,left} + Z_{r,left} + Z_{f,right} + Z_{r,right}}{4} - b_e, \tag{13}$$

$$\tan\beta_y = \frac{Z_{r,left} - Z_{f,left} + Z_{r,right} - Z_{f,right}}{2l_s}, \tag{14}$$

$$\tan\beta_x = \frac{Z_{f,left} - Z_{f,right} + Z_{r,left} - Z_{r,right}}{2\,(2b_{EC})}. \tag{15}$$

In general, the simple form with two parallel tandems, shown in Fig. 7, is not sufficient to obtain accurate results for sharp irregularities. Therefore, more parallel tandems and intermediate cams are added, as illustrated by Fig. 8. Specifically, parallel tandems are added along the tire's width, while the intermediate cams are positioned between the front and rear edge of the tire contact patch. In addition, the intermediate cams between the left and right sides are not necessary since their contribution cancel out when calculating the effective road camber angle [29]. The same equations, as presented earlier for the simple 3D enveloping contact model, apply again, but now extended for the case of multiple parallel tandems and intermediate cams. In particular, the three necessary quantities are provided by the expressions

$$w' = \frac{1}{n}\sum_{j=1}^{n}\left(\frac{Z_{fj} + Z_{rj}}{2}\right) - b_e, \tag{16}$$

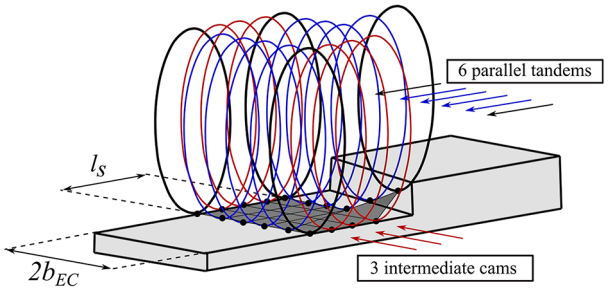

Fig. 8 3D enveloping contact model with n = *6 parallel tandems and m = 5 longitudinal cams* (*reproduced from* [28])

$$\tan\beta_y = \frac{1}{n}\sum_{j=1}^{n}\left(\frac{Z_{rj} - Z_{fj}}{l_s}\right), \tag{17}$$

$$\tan\beta_x = \frac{1}{m}\sum_{i=1}^{m}\left(\frac{Z_{i,n} - Z_{i,1}}{2b_{EC}}\right), \tag{18}$$

where m is the number of longitudinal cams and n is the number of parallel tandems.

The advantage of this contact model stems from its ability to provide improved accuracy in cases of short wavelengths (sharp steps) in the road height. However, it constitutes a more computationally demanding methodology in comparison to the above-presented RBF interpolation method. It should be emphasized that in this work it is possible to define which of the tires of a model (if any) will use the 3D enveloping contact method. Therefore, both tires that use the RBF interpolation method and the 3D enveloping contact model can co-exist in a model, leading to an optimum combination of accuracy and computational efficiency.

4 Tire–road interaction

In this section, the theoretical approach of this paper is completed by displaying the essential parts of the tire–soil interaction. Specifically, the soil modeling is initially presented, followed by the description of the normal and shear stress distribution over the tire–soil contact patch area. Subsequently, the equations for the modeling of the bulldozing resistance are presented, while the methodology used to take into account the tire deformability is explained next. Lastly, the core idea and the equations used for the multi-pass effect are illustrated at the final part of this section.

4.1 Soil modeling

The soil model is based on the classical and well-established expression introduced by Bekker for the pressure–sinkage relationship. More specifically, the pressure is derived by employing the Bekker formula [12, 13]

$$\sigma\,(h) = \left(\frac{k_c}{b} + k_\phi\right) h^n, \tag{19}$$

where b is the length of the shorter side of the rectangular contact patch, h is the sinkage, and k_c, k_φ, and n represent empirical coefficients. Moreover, regarding the soil failure, a variety

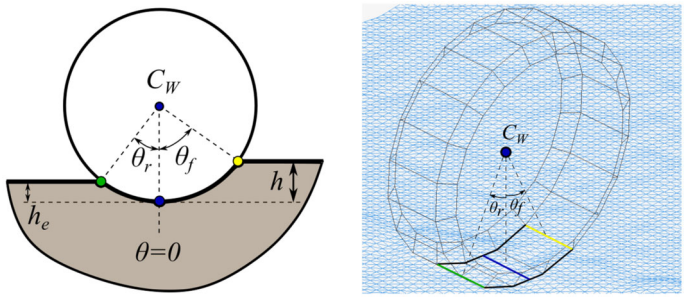

Fig. 9 Wheel contact angles and contact patch area

of criteria exist in the literature. Here, the widely used Mohr–Coulomb failure criterion is employed, which states that the maximum soil shear strength is provided by the expression

$$\tau_{\max,s}(\sigma) = c + \sigma \tan\phi, \tag{20}$$

where c is the soil apparent cohesion and φ is the angle of internal shearing resistance of the soil material.

4.2 Contact patch area

First, the tire–soil contact patch area, which is defined by the entry angle θ_f and the exit angle θ_r, is determined as a function of the sinkage h, the tire's radius R, and the elastic sinkage h_e by employing the equations

$$\theta_f = \cos^{-1}(1 - h/R), \tag{21}$$

$$\theta_r = \cos^{-1}(1 - h_e/R). \tag{22}$$

Specifically, the tire–soil contact patch constitutes the region defined by the wheel contact angles θ_f and θ_r in addition to the tire width, as shown in Fig. 9. Then, the springs enclosed in the contact patch area are, initially, identified. Subsequently, an effective road plane is constructed by using the soil elevation values of these springs, as explained in Sect. 3, through the determination of the equivalent soil elevation and local inclinations of the road surface.

4.3 Normal and shear stress distribution

Then, the normal and the shear stress distribution at the contact patch area is determined as a function of the wheel angle θ. More specifically, using the pressure–sinkage relationship proposed by Bekker (see Eq. (19)), the normal stress distribution is provided by

$$\sigma(\theta) = \begin{cases} R^n \left(\frac{k_c}{b} + k_\phi\right) \left(\cos\theta - \cos\theta_f\right)^n, & \theta_m \le \theta \le \theta_f \\ R^n \left(\frac{k_c}{b} + k_\phi\right) \left(\cos\left(\theta_f - \frac{\theta - \theta_r}{\theta_m - \theta_r}\left(\theta_f - \theta_m\right)\right) - \cos\theta_f\right)^n, & \theta_r \le \theta \le \theta_m \end{cases}, \tag{23}$$

where n is the sinkage exponent defined in Eq. (19). In the above equation, the parameter θ_m represents the wheel angle at which the normal stress is maximized, given by the formula [14]

$$\theta_m = (c_1 + c_2\kappa)\,\theta_f, \tag{24}$$

where c_1 and c_2 denote parameters that depend on the wheel–soil interaction and κ represents the longitudinal slip. Furthermore, the normal stress distribution, given by Eq. (23), is modified in this work to account for the soil damping effect [8]. Specifically, the normal stress distribution is provided by

$$\sigma(\theta) = \begin{cases} R^n \left(\frac{k_c}{b} + k_\phi\right) \left(\cos\theta - \cos\theta_f\right)^n + \frac{c_s v_c}{A_c}, & \theta_m \le \theta \le \theta_f \\ R^n \left(\frac{k_c}{b} + k_\phi\right) \left(\cos\left(\theta_f - \frac{\theta - \theta_r}{\theta_m - \theta_r}\left(\theta_f - \theta_m\right)\right) - \cos\theta_f\right)^n + \frac{c_s v_c}{A_c}, & \theta_r \le \theta \le \theta_m \end{cases} \tag{25}$$

where c_s denotes the soil damping, v_c represents the soil's compression rate/velocity, and A_c is the contact patch area.

Following that, the shear stress distributions $\tau_x(\theta)$ and $\tau_y(\theta)$, in the longitudinal (x) and in the lateral (y) direction respectively, are calculated using the similar expressions [15, 16]

$$\tau_x(\theta) = \tau_{\max}\left(1 - \exp\left(-\frac{j_x(\theta)}{k_x}\right)\right), \tag{26}$$

$$\tau_y(\theta) = \tau_{\max}\left(1 - \exp\left(-\frac{j_y(\theta)}{k_y}\right)\right). \tag{27}$$

In the above equations, the parameters k_x and k_y represent the shear modules, which are provided by the equations [17]

$$k_x = k_{x0}\alpha + k_{x1}, \tag{28}$$

$$k_y = k_{y0}\alpha + k_{y1}, \tag{29}$$

where α denotes the slip angle. Moreover, the soil deformations j_x and j_y are derived as functions of the wheel angle θ by employing the expressions [14, 16]

$$j_x(\theta) = R\left[\theta_f - \theta - (1-\kappa)\left(\sin\theta_f - \sin\theta\right)\right], \tag{30}$$

$$j_y(\theta) = R(1-\kappa)\left(\theta_f - \theta\right)\tan\alpha. \tag{31}$$

It should be emphasized that, for the maximum shear stress τ_{max} (see Eqs. (26)–(27)), a modified approach is followed here to take into account the coefficient of friction at the tire–soil interface [19]. More specifically, the maximum shear stress at the tire–soil interface $\tau_{max,\,ts}$ is initially approximated as a function of the pressure σ and the friction coefficient μ_s by employing the equation

$$\tau_{\max,ts}(\sigma) = \mu_s \sigma. \tag{32}$$

Subsequently, the minimum of the two constituent parts, namely the maximum soil shear strength (see Eq. (20)) and the maximum shear stress at the tire–soil interface is utilized here for the shear stress calculation [19]. That is,

$$\tau_{\max}(\sigma) = \min\left(\mu_s\sigma, c + \sigma\tan\phi\right). \tag{33}$$

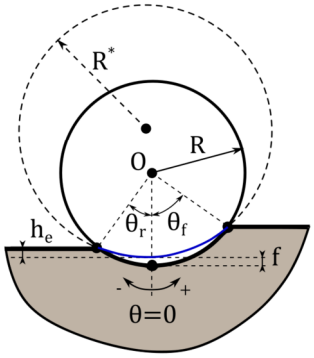

Fig. 10 Substitute circle method to account for the tire's deformability

4.4 Bulldozing resistance

Moreover, in this work, the lateral force comprises two different parts. Specifically, apart from the shear force exerted on the contact patch due to the tangential stresses τ_y, the bulldozing force, which acts on the side face of the wheel, due to the tire's sinkage, is also incorporated [16, 17]. Herein, the Hegedus resistance estimation method is used to calculate the bulldozing force [16, 17]. Using this approach, a bulldozing resistance R_b is developed per unit width of a blade, which is given by the equation

$$R_b = \frac{\cot X_c + \tan\left(X_c + \phi\right)}{1 - \tan\alpha' \tan\left(X_c + \phi\right)} \left\{ hc + \frac{1}{2}\rho_s h^2 \left[\left(\cot X_c - \tan\alpha'\right) + \frac{\left(\cot X_c - \tan\alpha'\right)^2}{\tan\alpha' + \cot\phi} \right] \right\}, \tag{34}$$

where ρ_s is the soil density. Moreover, the destructive angle X_c, based on Bekker's theory, is approximated by

$$X_c = 45^\circ - \frac{\phi}{2}. \tag{35}$$

4.5 Tire deformability

To account for the tire's deformability, a larger substitute circle is used to describe the tire–soil contact patch area [13, 19, 32], as shown in Fig. 10. More specifically, to calculate the diameter of the substitute circle, an iterative procedure is followed until the soil vertical reaction force and the tire vertical force are balanced. The former is calculated through integration of the normal and shear stresses at the contact patch area, while for the latter, the tire's vertical stiffness is used along with the corresponding deformation. More specifically, the soil vertical reaction force is given by

$$F_{z,s} = bR^* \int_{\theta_r^*}^{\theta_f^*} \left[\tau_x\left(\theta^*\right) \sin\theta^* + \sigma\left(\theta^*\right) \cos\theta^* \right] d\theta^*, \tag{36}$$

while the tire vertical force is provided by

$$F_{z,t} = K_t f, \tag{37}$$

where K_t denotes the tire's vertical stiffness and f stands for the resulting deformation of the tire. In addition, an extra equation is needed, which relates the tire's deformation and the

radius of the substitute circle R^*. For this, the following expression, originally proposed by Bekker, is used:

$$\frac{R^*}{R} = \left(\sqrt{1+\frac{f}{h}} + \sqrt{\frac{f}{h}}\right)^2. \tag{38}$$

The last three equations are solved iteratively until

$$\left|F_{z,s} - F_{z,t}\right| < \varepsilon_F, \tag{39}$$

where the value of the numerical threshold ε_F constitutes a function of the tire's maximum vertical load. Specifically, for a given value of the tire sinkage, which is easily determined based on the wheel's position at each time point, the resulting tire deformation f and the radius of the substitute circle R^* must be calculated so that the forces given by Eqs. (36) and (37) will be in balance. In particular, the value of the tire deformation is, initially, modified. Then, the radius of the substitute circle R^* is determined by using Eq. (38). Subsequently, the forces given by Eqs. (36) and (37) are calculated, and the condition given by Eq. (39) is evaluated. If this condition is not satisfied, then the value of the tire deformation is, again, modified and the above-described procedure is repeated.

It should be noted that, in cases of negligible deformation of the tire, an extra functionality can be enabled to model the tire as nondeformable (rigid) and, thus, simplify and accelerate the calculation of the vertical force F_z. Specifically, no iterations are required in this case since only Eq. (36) is used where the quantities R^* and θ^* are replaced by R and θ respectively.

4.6 Multi-pass effect

Lastly, regarding the multi-pass effect, the response of the soil to repetitive normal load needs to be established. More specifically, the mathematical description of the normal stress distribution must be modified in cases of existing precompaction of the soil [18, 19]. In general, one part of the induced soil deformation is elastic (elastic sinkage), and the remaining part (plastic sinkage) is irreversible. Therefore, a proper way to distinguish between these two constituent parts of the total sinkage needs to be established.

Within this work, the following equation is used for the calculation of the elastic sinkage:

$$h_e = \frac{\sigma\left(\theta_m\right)}{K_s}, \tag{40}$$

where K_s denotes the soil's elastic stiffness.

4.7 Soil library

In all semi-empirical soft soil tire models, the proper selection of the associated parameters is, undoubtedly, a challenging task from the user's perspective, while crucial for the development of reliable and accurate models at the same time. Specifically, some physical tests are, generally, required for the determination of these parameters. These experiments are very expensive, require special equipment, and take a significant amount of time to be executed.

Based on this, a ready-to-use soil library has already been created, which can be used as a very good starting point. The developed soil library, which is based on the existing literature [1, 14, 17, 18, 33], includes the associated properties for a variety of soil types. Then, the

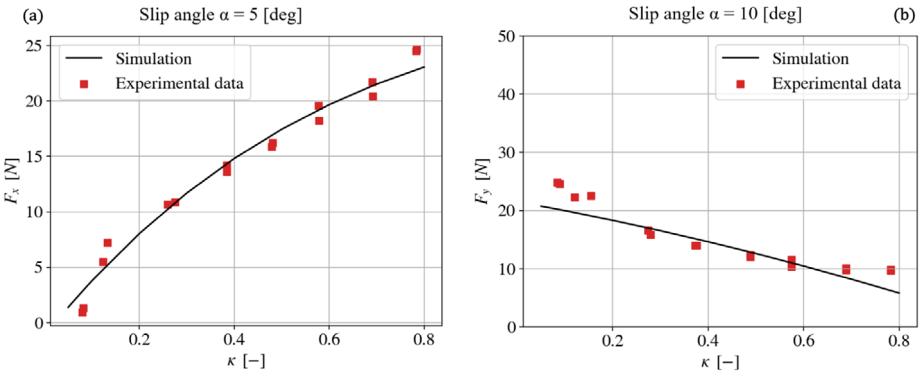

Fig. 11 Single-wheel test bed results under combined slip conditions: (*a*) *Longitudinal force – Longitudinal slip for* $\alpha = 5$ $[deg]$ *and* (*b*) *Lateral force – Longitudinal slip for* $\alpha = 10$ $[deg]$ (*source of experimental data:* [17])

default values for the relevant properties can be modified if the user has some additional knowledge on the specific soil type used. Lastly, it should be noted that the developed soil library is already integrated into Altair's multi-body simulation software, MotionSolve.

5 Numerical results and discussion

In the current section, a full set of numerical results is presented to demonstrate the validity and effectiveness of the new methods. In particular, a single wheel test bed is initially examined, followed by a planetary exploration rover. Then, the FED-Alpha vehicle of the next generation NATO reference mobility model is tested in various complex maneuvers. Lastly, an advanced simulation involving both wheeled and tracked vehicles, namely a utility terrain vehicle and a personnel carrier vehicle, is also carried out by employing a shared road model.

5.1 Single-wheel test bed

To start with, the single tire's longitudinal and lateral forces are validated under combined slip conditions. Specifically, in Fig. 11 (a), the simulation results (MotionSolve) for the longitudinal force as a function of the longitudinal slip are compared with the corresponding experimental data [17] for the case of slip angle equal to 5 degrees. Similarly, in Fig. 11 (b), the lateral force is examined for the case of slip angle equal to 10 degrees.

5.2 Planetary exploration rover

Next, a four-wheeled planetary exploration rover [17] is examined in various maneuvers. This vehicle, shown in Fig. 12, consists of eleven (11) bodies and ten (10) joints in total, while the wheels are connected to the main body through rocker suspension. In addition, all four wheels of the rover possess a steering degree of freedom.

First, a steering maneuver is examined where the front wheels are steered by 30 degrees. Specifically, in Fig. 13 (a), the main body's center of mass x and y position is shown, while in Fig. 13 (b), the vehicle's yaw angle as a function of the simulation time is presented. As

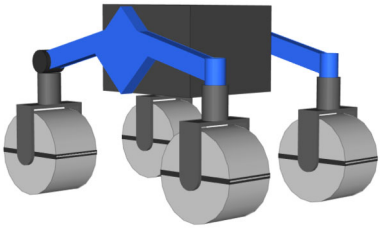

Fig. 12 MotionView model of four-wheeled planetary exploration rover

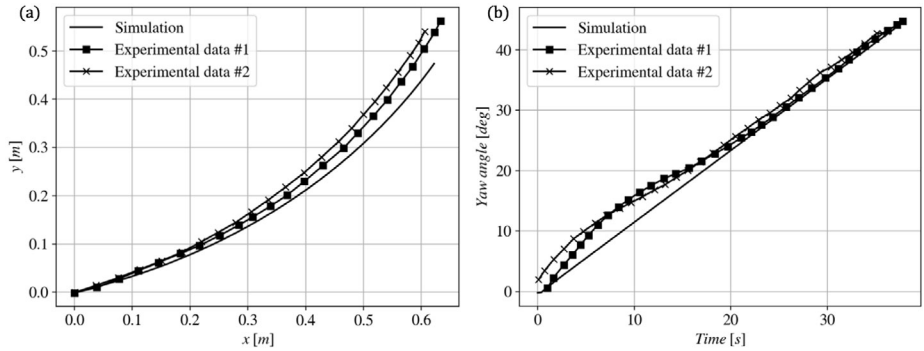

Fig. 13 Steering maneuver results: (*a*) *Main body's center of mass position and* (*b*) *Vehicle's yaw angle – Simulation time* (*source of experimental data:* [17])

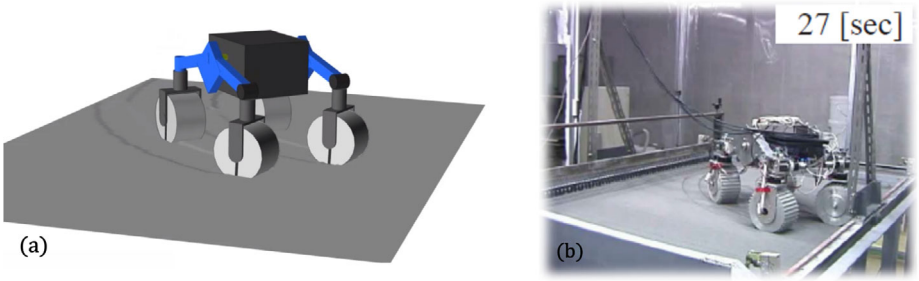

Fig. 14 Path of the vehicle and resulting soil compaction for the steering maneuver

can be seen from both graphs, a very good correlation is achieved between the simulation results and the corresponding experimental data [17].

Moreover, the path of the vehicle and the resulting soil compaction are illustrated in Fig. 14 both for the simulated and the experimental case. It should also be emphasized that the total simulation time of this maneuver is 37 [s], while the necessary CPU time is 35.33 [s]. The simulation was performed by using a single core of an Intel® Core™ i7-10875H Processor @ 2.30 GHz. Therefore, it is of great interest that the CPU time is comparable with the simulation time, even by using a single core for running the simulation.

Until this point, a flat road surface was used in all examined cases. Using this as a solid starting point, the developed soft-soil tire model is also validated and tested in much more complex terrain geometries. To start with, a slope traversing maneuver with a slope angle of 10 degrees is examined in Fig. 15. In particular, the simulation results for the main body's

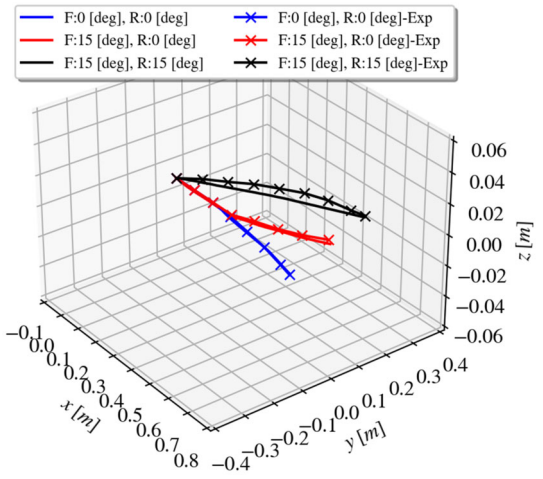

Fig. 15 Slope traversing maneuver ($\psi = 10\ [deg]$)*: Comparison of simulation results and experimental data* (*source of experimental data:* [34])

center of mass position are compared with the corresponding experimental data for three different cases [34]. Specifically, for the case marked with the blue curve, none of the four wheels of the rover model is steered, whereas only the front wheels are steered by 15 degrees for the case denoted with the red curve. Similarly, all four wheels of the rover model are steered by 15 degrees for the case marked with the black curve. Moreover, the necessary CPU time for this maneuver is 37.59 [s], whereas the total simulation time is 12.5 [s]. Again, it should be highlighted that the CPU time is comparable with the simulation time, even by using a single core, thus illustrating the computational efficiency of the proposed methods.

Regarding the numerical values of the soil properties for both the single-wheel test bed and the exploration rover simulation cases, the vast majority is provided by the corresponding publications, which include the experimental data [17, 34]. In addition, the soil's elastic stiffness K_s is determined by taking into account that the wheel sinkage ratio is approximately equal to 1 according to [17]. The coefficient of friction is selected equal to 0.8 based on the acceptable ranges derived from previous experimental observations [35], while the soil damping value is equal to 0.5 [kNs/m]. Lastly, the RBF interpolation method was used in these maneuvers for modeling the tire–soil contact.

5.3 Next generation NATO reference mobility model (NG-NRMM)

Following that, the capabilities of the proposed soft-soil tire model are also demonstrated by using available experimental data from the next generation NATO reference mobility model [31]. For this, the FED-Alpha vehicle is initially modelled in MotionView, as shown in Fig. 16. This vehicle model consists of 101 bodies and 97 joints in total, while double wishbone suspensions with air-springs, coil springs, and selective damper are employed. Then, a series of advanced soft terrain tests is used to demonstrate the effectiveness of the proposed methods in complex, real-life applications.

Specifically, the model representation is grouped in different subsystems corresponding to the same assemblies in the actual FED-Alpha vehicle. The relatively large number of bodies and joints is justified by the complexity of the examined vehicle and the necessity of providing an accurate description of all subsystems to capture the dynamic behavior of the vehicle in the best possible way. In particular, the majority of bodies and joints correspond to the suspension and driveline subsystems. For instance, the suspension stabilizer bar consists

Fig. 16 Model of FED-Alpha vehicle in MotionView

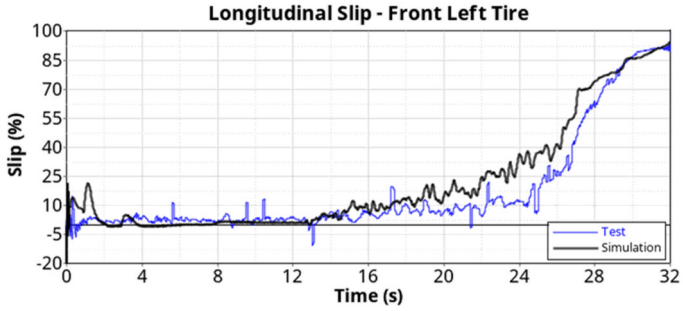

Fig. 17 Variable slope climbing maneuver: Comparison of simulation results and experimental data (*source of experimental data:* [31])

of a series of bodies that are properly connected through joints, thus leading to a significant number of bodies and joints for the suspension subsystem. Similarly, the need for an accurate representation of the center, front, and rear differentials (all-wheel drive configuration) leads to a significant number of bodies and joints for the driveline subsystem.

Specifically, a variable slope climbing maneuver is initially performed on dry sand soil terrain. In this case, a rough road surface is encountered and the slope grade is gradually increased from 0% up to approximately 30%. In Fig. 17, a comparison of the simulation and the experimental results for the longitudinal slip of the front left tire is carried out. However, since a locked differential is used for performing this maneuver, this slip value also corresponds to the average wheel slip.

As can be seen, a very good agreement is observed between the simulation results and the respective experimental data. In addition, a rough terrain surface is encountered in this case, as shown in Fig. 18. Therefore, the 3D enveloping contact model is used for all four wheels of the vehicle for this simulation. Moreover, the resulting soil plastic sinkage can be clearly observed in the same figure.

In addition, a drawbar pull experiment is also performed on dry sand soil surface. In particular, the results of the drawbar pull as a function of the average longitudinal slip is presented in Fig. 19 for the simulation and the physical experiment. In this case, the RBF interpolation method is employed for modeling the resulting tire–soil contact since a flat terrain is used for the drawbar pull experiment. Based on Figs. 17 and 19, the effectiveness and applicability of the proposed methods is highlighted, even for cases of such complex vehicle models and terrain geometries.

Fig. 18 Variable slope climbing maneuver: Terrain surface and resulting soil plastic sinkage

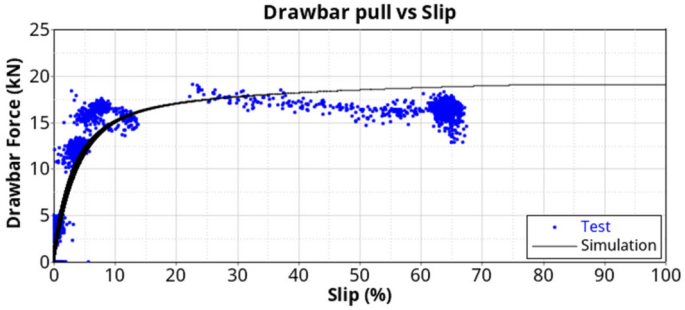

Fig. 19 Drawbar pull experiment on dry sand soil surface: Comparison of simulation results and experimental data (*source of experimental data:* [31])

Concerning the numerical values of the soil properties, the vast majority is provided by the test data extracted during the NG-NRMM's cooperative demonstration of technology event [31]. Moreover, the parameters c_1 and c_2 are chosen equal to 0.3 and 0.32, respectively, according to [14], while the coefficient of friction is set equal to 0.4. Lastly, the soil damping value is chosen equal to 0.5 [kNs/m].

5.4 Wheeled and tracked vehicles – shared road model

Lastly, an advanced simulation that includes all the presented features is examined. Specifically, a complex road surface with generic-shaped obstacles is used, as shown in Fig. 20 (c). The terrain corresponds to dry sand soil type, and the numerical values of the necessary soil properties are selected according to [18]. In addition, both wheeled and tracked vehicles co-exist in this model. In particular, a utility terrain vehicle (UTV) and a tracked personnel

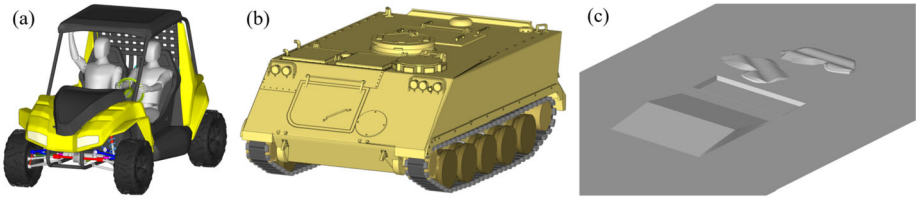

Fig. 20 The constituent parts of the examined model: (*a*) *Utility terrain vehicle*, (*b*) *Tracked personnel carrier vehicle, and* (*c*) *Road surface with generic-shaped obstacles*

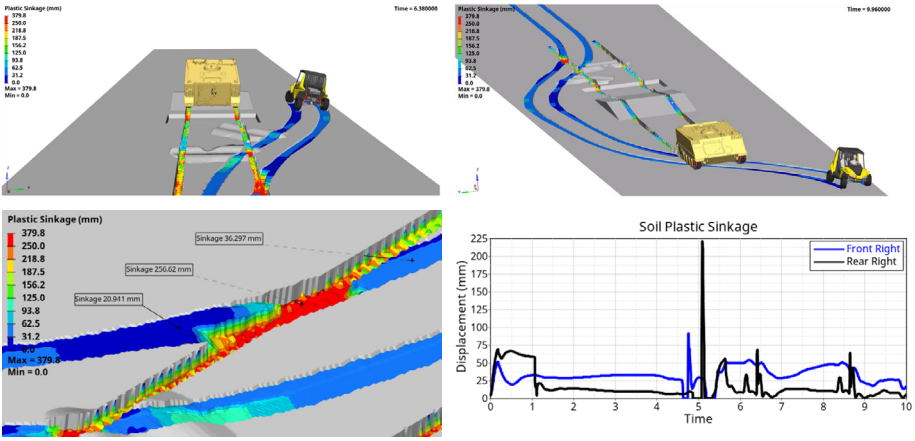

Fig. 21 Multi-pass effect – Road surface with generic-shaped obstacles: Resulting soil plastic sinkage in shared road model

carrier vehicle are employed, as illustrated in Fig. 20 (a), (b). Consequently, it should be noted that a generalization of the presented methods was performed for the case of tracked vehicles and for models including both wheeled and tracked vehicles through a shared road model.

The examined model consists of 379 bodies and 389 joints, in total. Moreover, 854 contact pairs are defined, while the total number of bushings and forces used in this model is 398. Concerning the results of the analysis, the multi-pass effect is clearly demonstrated by observing the plastic sinkage resulting both from the UTV and from the tracked vehicle (see Fig. 21). In addition, both vehicles interact with the generic-shaped obstacles during their course.

6 Conclusions

In the present study, a holistic approach for the simulation of wheeled vehicles on soft-soil terrain was proposed. For this, a new, fast, and memory-efficient road and contact model was developed. In addition, a generalization of the presented methods was also performed for tracked vehicles and for the cases where both wheeled and tracked vehicles co-exist in a model and, thus, a shared road model must be employed. Using the proposed methods, real-life applications involving complex phenomena can be properly handled.

Specifically, a distinct feature of the new road model stems from its ability to handle large road scenarios by allocating the memory for each spring when it is first needed, resulting in low memory allocation of the simulation code. Moreover, the height-field data structure is augmented with the soil properties and the soil compaction parameters in this work, while the rectangular grid structure used here leads to fast execution of the code. It is also worth noting that it is possible to define generic-shaped obstacles with different soft-soil properties in comparison to the whole soil area.

Subsequently, a computationally efficient tire–soil contact model, which enables the use of rough terrain geometries, was also presented here. More specifically, two different approaches were developed, namely the radial basis function interpolation method and the 3D enveloping contact model. Nonetheless, the core idea in both cases remains the same. That is, both contact models use the springs enclosed in the tire contact patch area to derive a proper equivalent plane and, thus, to provide the corresponding soil elevation and local inclinations of the road surface.

Finally, the proposed methods were implemented in Altair's multi-body simulation software MotionSolve, and numerous engineering problems were examined to demonstrate their effectiveness and applicability in complex real-life applications. In particular, a detailed validation of the proposed soft-soil tire model was initially performed by using available experimental data. In all cases, a very good agreement was observed between the simulation results and the corresponding experimental data. Moreover, the developed model was tested in various advanced maneuvers, incorporating rough terrain geometries, passing over obstacles, and the phenomena related to the multi-pass effect. Lastly, a variety of wheeled and tracked vehicle models was used in these maneuvers, including a planetary exploration rover, a utility terrain vehicle, the FED-Alpha vehicle, and a tracked personnel carrier vehicle.

Acknowledgements This research was funded by Altair Engineering Inc.

Author contributions E.K. developed the numerical methodology, wrote the corresponding codes, run the numerical results and wrote the original manuscript text. S.N. helped in the development and application of the numerical methodology. F.M., A.R. and S.N. helped in the selection of the mechanical examples, the development of the corresponding mechanical models and reviewed the final manuscript.

Funding Open access funding provided by HEAL-Link Greece.

Data Availability No datasets were generated or analysed during the current study.

Declarations

Competing interests The authors declare no competing interests.

References

1. Battiato, A.: Soil-tyre interaction analysis for agricultural tractors: Modelling of traction performance and soil damage (2014)

2. Yoshida, K., Watanabe, T., Mizuno, N., Ishigami, G.: Terramechanics-based analysis and traction control of a lunar/planetary rover. In: Field and Service Robotics, pp. 225–234. Springer, Berlin (2006)
3. Azimi, A., Kovecses, J., Angeles, J.: Wheel-soil interaction model for rover simulation and analysis using elastoplasticity theory. IEEE Trans. Robot. **29**, 1271–1288 (2013). https://doi.org/10.1109/TRO.2013.2267972
4. Edwards, B.: Co-simulation of mbd models with dem code to predict mobility on soft soil. In: 2018 NDIA Ground Vehicle Systems Engineering and Technology Symposium (2018)
5. Tasora, A., Mangoni, D., Negrut, D., Serban, R., Jayakumar, P.: Deformable soil with adaptive level of detail for tracked and wheeled vehicles. Int. J. Veh. Perform. **5**, 60–76 (2019). https://doi.org/10.1504/IJVP.2019.097098
6. Recuero, A., Serban, R., Peterson, B., Sugiyama, H., Jayakumar, P., Negrut, D.: A high-fidelity approach for vehicle mobility simulation: nonlinear finite element tires operating on granular material. J. Terramech. **72**, 39–54 (2017). https://doi.org/10.1016/j.jterra.2017.04.002
7. Serban, R., Olsen, N., Negrut, D., Recuero, A., Jayakumar, P.: A co-simulation framework for high-performance, high-fidelity simulation of ground vehicle-terrain interaction. In: Conference: NATO AVT-265 Specialists' Meeting, Vilnius, Lithuania (2017)
8. Li, H.: Analysis of Off-Road Tire-Soil Interaction Through Analytical and Finite Element Methods (2013)
9. Xia, K.: Finite element modeling of tire/terrain interaction: application to predicting soil compaction and tire mobility. J. Terramech. **48**, 113–123 (2011). https://doi.org/10.1016/j.jterra.2010.05.001
10. Hu, W., Rakhsha, M., Yang, L., Kamrin, K., Negrut, D.: Modeling granular material dynamics and its two-way coupling with moving solid bodies using a continuum representation and the SPH method. Comput. Methods Appl. Mech. Eng. **385** (2021). https://doi.org/10.1016/j.cma.2021.114022
11. Hu, W., Zhou, Z., Chandler, S., Apostolopoulos, D., Kamrin, K., Serban, R., Negrut, D.: Traction control design for off-road mobility using an SPH-DAE cosimulation framework. Multibody Syst. Dyn. **55**, 165–188 (2022). https://doi.org/10.1007/s11044-022-09815-2
12. Bekker, M.G.: Theory of Land Locomotion: The Mechanics of Vehicle Mobility. University of Michigan Press, Ann Arbor (1956)
13. Bekker, M.G.: Introduction to Terrain-Vehicle Systems. University of Michigan Press, Ann Arbor (1969)
14. Wong, J.-Y., Reece, A.R.: Prediction of rigid wheel performance based on the analysis of soil-wheel stresses. Part I. Performance of driven rigid wheels. J. Terramech. **4**, 81–98 (1967)
15. Janosi, Z., Hanamoto, B.: The analytical determination of drawbar pull as a function of slip for tracked vehicles in deformable soils. In: Proc. of 1st Int. Conf. of ISTVS, Turin (1961)
16. Yoshida, K., Ishigami, G.: Steering characteristics of a rigid wheel for exploration on loose soil. In: 2004 IEEE/RSJ International Conference on Intelligent Robots and Systems (IROS), pp. 3995–4000 (2004)
17. Ishigami, G., Miwa, A., Nagatani, K., Yoshida, K.: Terramechanics-based model for steering maneuver of planetary exploration rovers on loose soil. J. Field Robot. **24**, 233–250 (2007). https://doi.org/10.1002/rob.20187
18. Wong, J.Y.: Theory of Ground Vehicles. Wiley, New York (2008)
19. Harnisch, C., Lach, B., Jakobs, R., Troulis, M., Nehls, O.: A new tyre-soil interaction model for vehicle simulation on deformable ground. Veh. Syst. Dyn. **43**, 384–394 (2005). https://doi.org/10.1080/00423110500139981
20. Sandu, C., Taheri, S., Taheri, S., Gorsich, D.: Hybrid Soft Soil Tire Model (HSSTM). Part II: Tire-terrain interaction. J. Terramech. **86**, 15–29 (2019). https://doi.org/10.1016/j.jterra.2019.08.004
21. Senatore, C., Sandu, C.: Off-road tire modeling and the multi-pass effect for vehicle dynamics simulation. J. Terramech. **48**, 265–276 (2011). https://doi.org/10.1016/j.jterra.2011.06.006
22. Holm, I.C.: Multi-pass behaviour of pneumatic tires. J. Terramech. **6**, 47–71 (1969)
23. Krenn, R., Gibbesch, A.: Soft soil contact modeling technique for multi-body system simulation. In: Trends in Computational Contact Mechanics, pp. 135–155. Springer, Berlin (2011)
24. Azimi, A., Holz, D., Kövecses, J., Angeles, J., Teichmann, M.: Efficient dynamics modeling for rover simulation on soft terrain. In: 50th AIAA Aerospace Sciences Meeting Including the New Horizons Forum and Aerospace Exposition (2012)
25. Azimi, A.: Wheel-soil interaction modelling for rover simulation and analysis (2013)
26. Buhmann, M.D.: Radial Basis Functions: Theory and Implementations. Cambridge University Press, Cambridge (2003)
27. Mai-Duy, N., Tran-Cong, T.: Approximation of function and its derivatives using radial basis function networks. Appl. Math. Model. **27**, 197–220 (2003)
28. Schmeitz, A.J.C.: A semi-empirical three-dimensional model of the pneumatic tyre rolling over arbitrarily uneven road surfaces (2004)
29. Pacejka, H.: Tire and Vehicle Dynamics. Elsevier, Amsterdam (2005)

30. McCullough, M., Jayakumar, P., Dasch, J., Gorsich, D.: The next generation NATO reference mobility model development. J. Terramech. **73**, 49–60 (2017). https://doi.org/10.1016/j.jterra.2017.06.002
31. Letherwood, M., Jayakumar, P., Gerth, R., Dasch, J.: Cooperative Demonstration of Technology (CDT) for Next-Generation NATO Reference Mobility Model (NG-NRMM) (2020)
32. Schmid, I.C.: Interaction of vehicle and terrain results from 10 years research at IKK. J. Terramech. **32**, 3–26 (1995)
33. Wong, J.Y.: Terramechanics and off-road vehicle engineering: terrain behaviour, off-road vehicle performance and design. Butterworth-Heinemann (2009)
34. Ishigami, G., Miwa, A., Nagatani, K., Yoshida, K.: Terramechanics-based analysis on slope traversability for a planetary exploration rover. In: Proceedings of the International Symposium on Space Technology and Science, p. 1025 (2006)
35. Sperling, F.B.: Basic and Mechanical Properties of the Lunar Soil Estimated from Surveyor Touchdown Data (1970)